nature communications

Article

https://doi.org/10.1038/s41467-025-63797-1

Orbital electron coupling of Ga-Cd dual-atom sites catalyzes sulfur redox in potassium-sulfur battery

Received: 2 October 2024

Accepted: 21 August 2025

Published online: 30 September 2025

Check for updates

Shipeng Zhang[1,2,5], Zhen Li[3,5], Menggang Li[1], Yu Gu[1], Ying Han[1], Ruijin Zeng[1], Lu Tao[1], Youxing Liu[1], Na Ye[1], Xiaocang Han[1], Mingchuan Luo[1], Xiaoxu Zhao[1], Yan Yu[3] ✉, Shaojun Guo[1] ✉ & Jin Zhang[1,4] ✉

Dual-atom catalysts are a class of important catalytic systems for accelerating the kinetics of solid-phase conversion of K_2S_2 to K_2S in potassium-sulfur battery cathodes, *yet* their uncontrolled metal-metal interactions greatly limit their catalytic capability, leading to low conversion efficiency of potassium-sulfur batteries. Herein, we report the precise synthesis of Ga-Cd dual-atom catalysts with strong orbital electron coupling of *p*-block Ga and *d*-block Cd, anchored on hollow mesoporous carbon spheres (Ga-Cd DAs-HMCS) for boosting the performance of potassium-sulfur batteries. Ga shows strong adsorption capacity for potassium polysulfides, but lacks sufficient valence electrons to promote their conversion. We demonstrate that the introduction of Cd with a more filled valence electron configuration enables the transfer of electrons into the empty orbitals of Ga via strong orbital electron coupling, which enhances the catalytic ability of the Ga site to activate the S-S bond in potassium-sulfur chemistry, and thus accelerates the conversion kinetics from K_2S_2 to K_2S. This enables a S/Ga-Cd DAs-HMCS cathode material with an improved rate performance up to 589 mAh g^{-1} at 5 A g^{-1}.

Because of their high theoretical specific energy (1023 Wh kg^{-1}), the multi-electron reaction capability of sulfur cathode, the low redox potential of K metal anode (−2.93 V *vs SHE*), and their cost-effectiveness, potassium-sulfur (K-S) batteries have emerged as a significant research area with the objective of developing efficient energy storage systems[1–8]. Nevertheless, challenges such as the low utilization of active sulfur, the larger ionic radius of K^+ compared to Li^+/Na^+, and the high conversion energy barrier associated with solid-state transformation from K_2S_2 to K_2S contribute to a low conversion efficiency of K-S batteries, resulting in substantial capacity loss[9–14]. It is therefore imperative to identify an optimal sulfur cathode catalyst capable of enhancing the solid-state potassium polysulfides conversion efficiency in the sulfur redox reaction and suppressing the "shuttle effect", which are the key to enhancing the value of K-S batteries[15].

Single atom, metal nanoparticles and polar compounds have been developed for improving the sluggish kinetics of K-S batteries[16–18]. However, the existing catalysts struggle to simultaneously catalyze and adsorb potassium polysulfide while promoting the migration of K^+. In particular, the solid-state conversion of K_2S_2 to K_2S is highly insulating and resistant to decomposition, which can readily accumulate on the catalytic sites, resulting in catalyst poisoning[19–22]. Dual-atom catalysts (DACs) with specific electronic redistribution have the potential to

[1]School of Materials Science and Engineering, Peking University, Beijing, China. [2]State Key Laboratory of Solidification Processing, Center for Nano Energy Materials, School of Materials Science and Engineering, Northwestern Polytechnical University and Shaanxi Joint Laboratory of Graphene (NPU), Xi'an, China. [3]Hefei National Research Center for Physical Sciences at the Microscale, Department of Materials Science and Engineering, University of Science and Technology of China, Hefei, Anhui, China. [4]Center for Nanochemistry, Beijing Science and Engineering Center for Nanocarbons, Beijing National Laboratory for Molecular Sciences, College of Chemistry and Molecular Engineering, Peking University, Beijing, China. [5]These authors contributed equally: Shipeng Zhang, Zhen Li. ✉e-mail: yanyumse@ustc.edu.cn; guosj@pku.edu.cn; jinzhang@pku.edu.cn

synergistically change the spatial configuration and electronic properties of two metal atoms for improving the sluggish conversion kinetics of K-S batteries[23–28]. However, to date, there are still grand challenges for the precise synthesis of a dual-atom catalytic system with strong atom-atom interaction, and also the clarification of their new electronic structure-catalytic efficiency relationship.

Herein, we present a class of heteronuclear Ga-Cd DACs with strong orbital electron coupling, anchored on hollow mesoporous carbon spheres (Ga-Cd DAs-HMCS), as a highly efficient catalyst for boosting the kinetics and stability of K-S batteries. Given their analogous orbital energies and shapes, the *p*-orbitals of Ga exhibit a greater tendency to hybridize with the *p*-orbitals of S, resulting in a stronger adsorption of potassium polysulfide at the Ga site. We investigate that the valence electron orbitals of the *d*-block Cd are highly filled, and possess a notable propensity for electron transfer to external entities. By leveraging the relatively abundant empty orbitals and the higher electronegativity of the *p*-block Ga, the *d*-block Cd is possible to facilitate a regular electron transfer to the empty orbitals of the Ga. Based on the controllable orbital electron coupling of Ga-Cd dual-atom sites, Ga as an active site could enhance the activation of the S-S bond in K_2S_2 and facilitate the conversion of solid-phase K_2S_2 to K_2S, resulting in a multifunctional catalyst with both adsorption and catalytic reduction capabilities. The as-prepared S/Ga-Cd DAs-HMCS cathode can provide a high rate performance (589 mAh g^{-1} at 5 A g^{-1}), discharge capacity (855 mAh g^{-1} at 0.2 A g^{-1} after 100 cycles) and cycling stability over 500 cycles at 1 A g^{-1}. The in situ X-ray diffraction (XRD), ex situ high-resolution X-ray photoelectron spectroscopy (XPS), ex situ high-resolution transmission electron microscopes (HRTEM) and in situ ultraviolet-visible (UV-vis) spectroscopy collectively reveal that the electrocatalysis mechanism of Ga-Cd DACs, highlighting how the orbital electron coupling facilitates the conversion of solid potassium polysulfide while inhibiting the "shuttle effect" associated with potassium polysulfide.

Results and discussion

Figure 1a illustrates the preparation of highly N-doped HMCS via a two-step coordination reaction involving Ga^{3+} and Cd^{2+} ions, following cryo-photo reduction. Specifically, it was synthesized by combining the polymerization of m-aminophenol and formaldehyde (APF) with a SiO_2 template, followed by calcination and NaOH etching. Due to the low melting point of Ga and the low boiling point of Cd, the Ga and Cd atoms are uniformly anchored onto the highly N-doped HMCS without the formation of metal clusters.

Scanning electron microscopy (SEM), high-angle annular dark-field scanning transmission electron microscopy (HAADF-STEM), and TEM were employed to elucidate the structural characteristics of the S/Ga-Cd DAs-HMCS. As shown in Fig. 1b & S1a, b, the Ga-Cd SiO_2@APF displays the uniform spherical structure with a diameter of around 200-300 nm. Figure 1c & S1c, d demonstrate the hollow porous characteristics of the Ga-Cd DAs-HMCS. The HAADF-STEM image (Fig. 1d) reveals numerous adjacent bright spots of varying shades for Ga-Cd DAs-HMCS. The corresponding 3D atom mapping of these pairs in Fig. 1e clearly illustrates the existence of heteronuclear atom pairs. The atom distances of these heteronuclear atom pairs were found to be approximately 4.19 Å (Fig. 1f), as identified by the intensity profiles of Fig. S2. Figure 1g presents the corresponding energy dispersive spectroscopy (EDS) mapping of Ga-Cd DAs-HMCS, revealing the uniform distribution of C, N, O, Ga, and Cd elements throughout the N-doped HMCS. The atomic-resolution HAADF-STEM image, corresponding mapping, and EDS patterns of line scanning of Ga-Cd DAs-HMCS further explain that the distributions of the Ga and Cd elements on the atomic-resolution and elemental content ratio of Ga and Cd (Fig. S3). Figure S4 displays the TEM, STEM images, and EDS mappings of S/Ga-Cd DAs-HMCS, confirming the uniform penetration of sulfur into the mesoporous and cavity regions of the N-doped HMCS. To investigate the charge transfer capacity within the Ga-Cd atom pair for catalyzing potassium polysulfide, we synthesized control samples of single-atom (SA) Ga and Cd anchored on HMCS (Ga SA-HMCS and Cd SA-HMCS), as well as a standard normal group of N-doped HMCS. Their SEM, TEM, STEM images, and EDS patterns of these three control samples were tested (Fig. S5–11). The atomic-resolution HAADF images of Ga SA-HMCS and Cd SA-HMCS reveal numerous bright spots on the HMCS surface (Figs. S12 & 13), attributed to single-atom Ga and Cd, respectively.

As shown in Fig. S14a, the Ga-Cd DAs-HMCS, Ga SA-HMCS, Cd SA-HMCS and HMCS show substantial quantities of both micropores and mesopores (0.5-4.1 nm). Following sulfur infusion, active sulfur was found to occupy these pore structures, effectively filling the porous network (Fig. S14b). The Brunauer-Emmett-Teller (BET) analysis indicates that the Ga-Cd DAs-HMCS (1217 m^2g^{-1}), Ga SA-HMCS (1152 m^2g^{-1}), Cd SA-HMCS (1254 m^2g^{-1}) and HMCS (1289 m^2g^{-1}) possess a large specific surface area (Fig. S14c, d). X-ray diffraction (XRD) patterns of Ga-Cd DAs-HMCS, Ga SA-HMCS, Cd SA-HMCS and HMCS reveal only a carbon diffraction peak (Fig. S15), indicating that the Ga and Cd nanoclusters are not present on the HMCS. Following the sulfur immobilization, the S/Ga-Cd DAs-HMCS, S/Ga SA-HMCS, S/Cd SA-HMCS and S/HMCS exhibit no discernible diffraction peaks. This observation suggests that sulfur molecules are uniformly dispersed within the mesoporous structure of the N-doped HMCS. The amount of Ga and Cd atoms in Ga-Cd DAs-HMCS was determined to be 2.36 wt % and 4.74 wt%, respectively, by inductively coupled plasma mass spectrometry (ICP-MS). The Ga atom in Ga SA-HMCS and the Cd atom in Cd SA-HMCS were determined to be 4.05 wt% and 5.14 wt%, respectively. The high elemental content proves that the Ga and Cd atoms are highly densely dispersed in the N-doped HMCS host. Thermogravimetric analysis (TGA) of the S/Ga-Cd DAs-HMCS, S/Ga SA-HMCS, S/Cd SA-HMCS and S/HMCS samples indicates sulfur mass contents of 55.3 wt %, 55.6 wt %, 55.2 wt % and 58.9 wt %, respectively (Fig. S16).

To identify the chemical environments and atomic structures of Ga and Cd sites, X-ray absorption near-edge structure (XANES) and X-ray absorption fine structure spectroscopy were performed on Ga-Cd DAs-HMCS, Ga SA-HMCS, Cd SA-HMCS, and standard references (Fig. 2a & b). The absorption edge energies of the Ga K-edge and Cd K-edge in Ga-Cd DAs-HMCS, Ga SA-HMCS, and Cd SA-HMCS are situated between the standard references of Ga foil and Ga_2O_3, as well as Cd foil and CdO, indicating the Ga and Cd oxidation states locate between Ga^0 and Ga^{III}, and Cd^0 and Cd^{II}, respectively[29–31]. The intensity of the Ga K-edge white line serves as a qualitative indicator of electron density in the 4*p* orbitals of Ga. The *inset* in Fig. 2a illustrates that the peak intensity of Ga-Cd DAs-HMCS is lower than that of Ga SA-HMCS, suggesting that the electron density of Ga-Cd DAs-HMCS is greater than that of Ga SA-HMCS. The *inset* in Fig. 2b presents an opposing result, indicating the electron jump from the 5*s* orbital of Cd to the 4*p* orbital of Ga, thereby confirming the electron transfer from Cd to Ga[32]. The Fourier transform (FT) k^2-weighted EXAFS spectra of Ga-Cd DAs-HMCS, Ga SA-HMCS, and Cd SA-HMCS exhibit distinct peaks at approximately 1.42 Å and 1.67 Å, respectively. No characteristic peaks corresponding to Ga-Ga or Cd-Cd bonds are detected, indicating the presence of isolated Ga-N and Cd-N coordination (Fig. 2c & d). The fitted parameters of the Ga and Cd K-edge for Ga-Cd DAs-HMCS are shown in Fig. 2e & S21a, Table S1 & 2, the coordination number (CN) and bond length of Ga and N are determined to be 4.2 and 1.9 Å, respectively, while for Cd and N, the CN and bond length are 4.2 and 2.3 Å, suggesting the formation of Ga-N_4 and Cd-N_4 sites on the HMCS. The EXAFS fitting curves and Wavelet transform (WT) EXAFS were performed on Ga-Cd DAs-HMCS, Ga SA-HMCS, Cd SA-HMCS, and standard references to provide both K- and R-space resolution, further elucidating the dispersion of Ga and Cd atoms on the HMCS (Fig. S17–24). The Ga-N-N-Cd structural model (*inset* in Fig. 2e) and the

https://doi.org/10.1038/s41467-025-63797-1

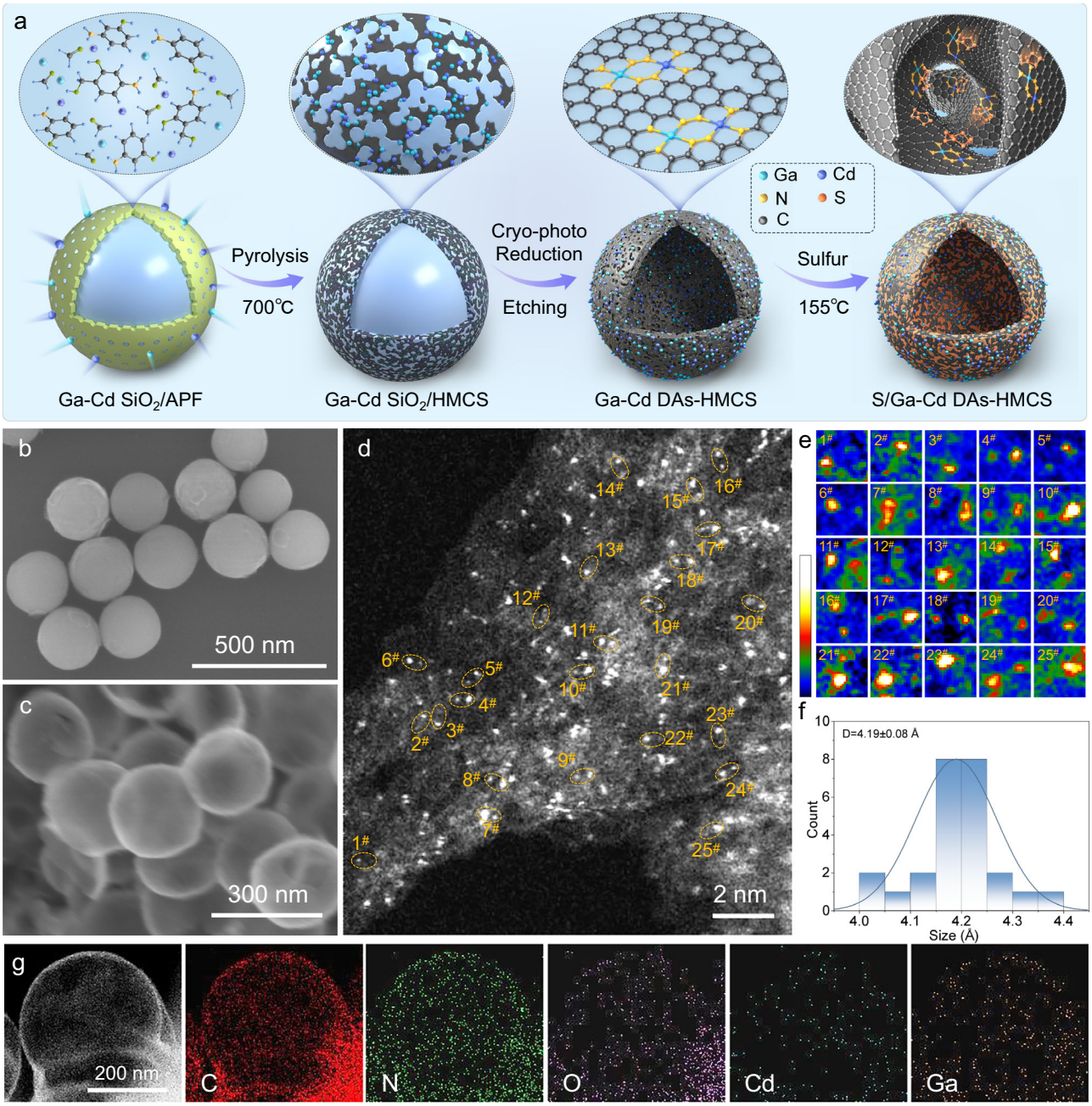

Fig. 1 | Synthesis and characterization of S/Ga-Cd DAs-HMCS. a Schematic illustration of the synthesis of S/Ga-Cd DAs-HMCS cathode. **b** SEM image of the Ga-Cd SiO_2/APF. **c** SEM and **d** atomic-resolution HAADF-STEM images of the Ga-Cd DAs-HMCS. **e**, **f** 3D atom mapping and atom distance of Ga-Cd atom pair for marked areas in (**d**). **g** EDS elemental mapping for C, N, O, Cd, and Ga elements of Ga-Cd DAs-HMCS. Source data for (**f**) was provided as a Source Data file.

interatomic distance of the Ga-Cd atom pair (~4.2 Å) are ascertained based on the aforementioned HAADF-STEM images and XAS results.

To further ascertain the interaction between the Ga and Cd atom pair and the surface elemental compositions and electronic states of the Ga-Cd DAs-HMCS, Ga SA-HMCS, and Cd SA-HMCS, the high-resolution XPS spectra were collected (Fig. S25–27). The full survey spectrum of Ga-Cd DAs-HMCS displays five types of characteristic peaks (C, N, O, Ga, and Cd elements) in the range of 200-1200 eV (Fig. S25a). The fitted N-Ga and N-Cd peaks in the high-resolution N 1*s* XPS spectra of Ga-Cd DAs-HMCS provide additional evidence for the coordination between the N atoms and the Ga/Cd atoms in this system (Fig. S25b). In Fig. 2f, the Ga $2p_{1/2}$ (1117.0 eV) and Ga $2p_{3/2}$ (1143.9 eV) peaks in Ga-Cd DAs-HMCS exhibit a downshift of ~0.2 eV compared to those in Ga SA-HMCS (Ga $2p_{1/2}$ at 1117.2 eV and Ga $2p_{3/2}$ at 1144.1 eV). In contrast, the XPS spectra of Cd 3 d for both Ga-Cd DAs-HMCS and Cd SA-HMCS (Fig. 2g) reveal that the Ga-Cd DAs-HMCS (Cd $2p_{3/2}$ at 404.7 eV and Cd $2p_{5/2}$ at 411.5 eV) exhibits a high energy shift of ~0.2 eV relative to the Cd SA-HMCS (Cd $2p_{3/2}$ at 404.5 eV and Cd $2p_{5/2}$ at 411.3 eV)[30,33]. These results indicate the electron transfer from the Cd atoms to the Ga atoms in the Ga-Cd DAs-HMCS, thereby identifying Ga atoms as the primary catalytic center via the orbital electron coupling within the Ga-Cd DAs-HMCS catalytic system.

The electronic structure and interaction mechanisms between the Ga and Cd sites were further investigated by the density of states (DOS) of the Ga-Cd DAs-HMCS, Ga SA-HMCS, and Cd SA-HMCS (Fig. 2h & S28). The electronic states of Cd are primarily distributed within the valence band, with minimal contribution near the Fermi level. This phenomenon can be attributed to the fully filled valence electron

https://doi.org/10.1038/s41467-025-63797-1

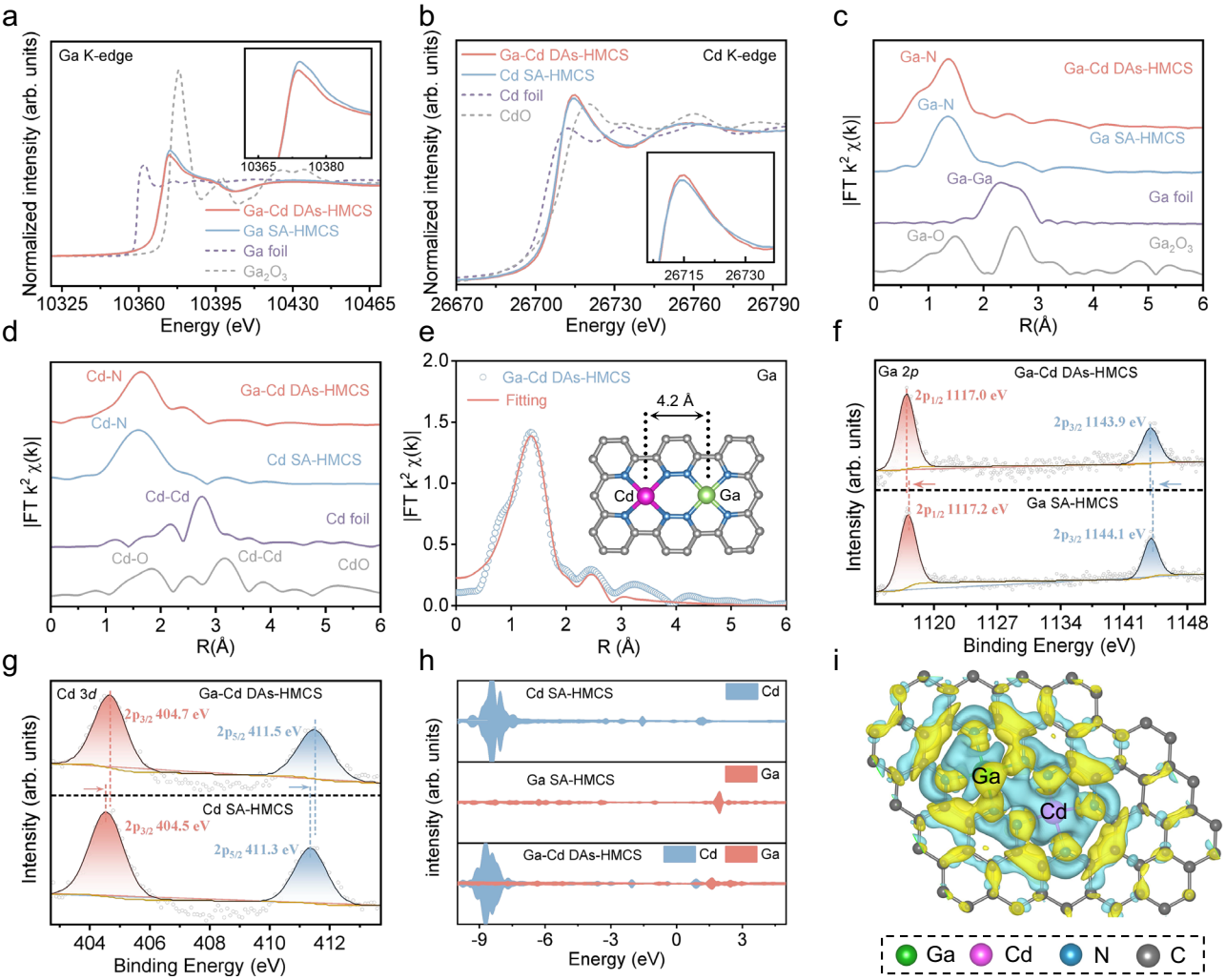

Fig. 2 | Electronic structures of Ga-Cd DAs-HMCS, Ga SA-HMCS and Cd SA-HMCS. a Ga K-edge XANES spectra of Ga-Cd DAs-HMCS, Ga SA-HMCS, Ga foil, and Ga_2O_3. **b** Cd K-edge XANES spectra of Ga-Cd DAs-HMCS, Cd SA-HMCS, Cd foil, and CdO. **c** Fourier-transform EXAFS spectra of Ga-Cd DAs-HMCS, Ga SA-HMCS, Ga foil, and Ga_2O_3. **d** Fourier-transform EXAFS spectra of Ga-Cd DAs-HMCS, Cd SA-HMCS, Cd foil, and CdO. **e** EXAFS fitting curve of Ga-Cd DAs-HMCS in R space (*Inset*: atomic structure of the Ga-Cd DAs-HMCS). **f** High-resolution XPS spectra of Ga 2*p* for Ga-Cd DAs-HMCS and Ga SA-HMCS. **g** High-resolution XPS spectra of Cd 3 *d* for Ga-Cd DAs-HMCS and Cd SA-HMCS. **h** The DOS of the Ga-Cd DAs-HMCS, Ga SA-HMCS and Cd SA-HMCS models. **i** The charge density difference of Ga-Cd DAs-HMCS model. Source data for **a**–**h** were provided as a Source Data file.

configuration of Cd ([Kr]$4d^{10}5s^2$), which hinders its coordination with potassium polysulfide. Conversely, the electronic states of Ga ([Ar] $3d^{10}4s^24p$) are mainly distributed above the Fermi energy level[34,35]. A comparison of the DOS between Ga-Cd DAs-HMCS and Ga SA-HMCS reveals a notable downward shift in the electronic states of Ga within the Ga-Cd atom pair relative to the Fermi level, proving that Cd can donate some electrons to the empty orbitals of Ga. Additionally, the introduction of Cd results in an electron gain for Ga over Cd, as evidenced by the charge density difference, further demonstrating the orbital electron coupling between the *p*-block Ga and the *d*-block Cd (Fig. 2i).

The unique orbital electron coupling between Ga atoms, which serve as the primary catalytic centers, enables the Ga-Cd DAs-HMCS to efficiently catalyze potassium polysulfide in K-S batteries in the potential window of 0.5-2.8 V (*vs.* K^+/K). The cyclic voltammograms (CVs) of the S/Ga-Cd DAs-HMCS, S/Ga SA-HMCS, S/Cd SA-HMCS, and S/HMCS were conducted at 0.1 mV s^{-1} for the first four cycles (Fig. 3a & S29). For the S/Ga-Cd DAs-HMCS cathode, the reduction peak at ~2.5 V corresponds to the formation of long-chain potassium polysulfides (e.g., K_2S_6 or K_2S_4), while two additional, more pronounced reduction peaks at ~1.14 V and ~0.73 V are attributed to the formation of insoluble short-chain potassium polysulfides of K_3S_2/K_2S_2 and K_2S. Compared to the S/Ga SA-HMCS, S/Cd SA-HMCS, and S/HMCS cathodes, the S/Ga-Cd DAs-HMCS exhibits the strongest oxidation peaks, indicating that it can effectively reduce the energy barrier of sulfur conversion via the non-bonding interaction of the Ga-Cd atom pair[36–38]. Furthermore, an analysis of the galvanostatic charge-discharge profiles during the first cycle suggests that the S/Ga-Cd DAs-HMCS demonstrates the highest Coulombic efficiency (CE) of ~56.7% (Fig. S30). Figure 3b shows the second galvanostatic charge-discharge profiles of the S/Ga-Cd DAs-HMCS cathode alongside the three control groups. Notably, the S/Ga-Cd DAs-HMCS cathode exhibits the lowest overpotential of ~0.95 V among all samples, including S/Ga SA-HMCS (~1.06 V), S/Cd SA-HMCS (~1.01 V), and S/HMCS (~1.23 V), indicating that Ga-Cd DACs can reduce the polarizing voltage during the redox reaction of sulfur.

The cycling and rate performance were examined to assess the stability and catalytic efficiency of the Ga-Cd DAs-HMCS electrocatalyst for K-S batteries. As illustrated in Fig. 3c, the S/Ga-Cd DAs-HMCS cathode exhibits the highest discharge capacity of 855 mAh g^{-1} at a specific current of 0.2 A g^{-1} after 100 cycles, surpassing the capacities of the S/Ga SA-HMCS (657 mAh g^{-1}), S/Cd SA-HMCS (590 mAh g^{-1}), and S/HMCS (355 mAh g^{-1}) cathodes. The electronic

https://doi.org/10.1038/s41467-025-63797-1

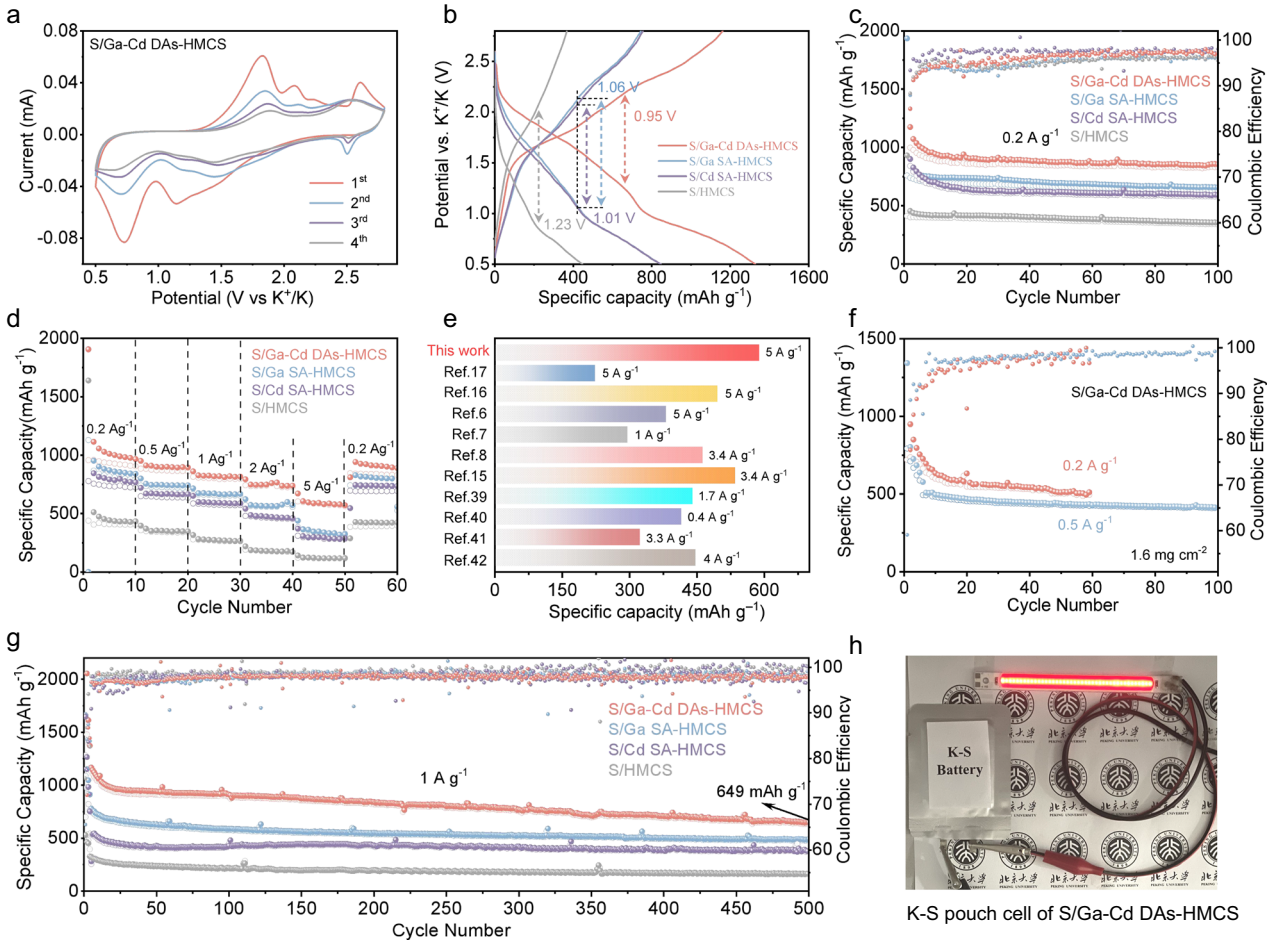

Fig. 3 | Electrochemical performance of S/Ga-Cd DAs-HMCS cathode and three control groups (S/Ga SA-HMCS, S/Cd SA-HMCS, and S/HMCS) for K-S batteries. **a** CVs of S/Ga-Cd DAs-HMCS cathode at a scan rate of 0.1 mV s^{-1}. **b** Galvanostatic charge-discharge curves at 0.2 A g^{-1}. **c** Cycle performance and **d** rate capabilities. **e** Comparison of S/Ga-Cd DAs-HMCS cathode at 5 A g^{-1} with previously reported cathodes for K-S batteries. **f** Cycling performance of S/Ga-Cd DAs-HMCS cathode with an S mass loading of 1.6 mg cm^{-2}. **g** Cycling stability at 1 A g^{-1}. **h** K-S pouch cell based on S/Ga-Cd DAs-HMCS cathode lighting LED. Source data for **a**–**g** were provided as a Source Data file.

effect of Cd on the regulation of Ga in the Ga-Cd DAs-HMCS as the catalytic active center enhances the conversion of potassium polysulfide, as evidenced by the strong rate performance (Fig. 3d). The S/Ga-Cd DAs-HMCS cathode demonstrates the highest discharge capacities of 1028, 901, 825, 747 and 589 mAh g^{-1} at 0.2, 0.5, 1, 2 and 5 A g^{-1}, respectively, compared to the S/Ga SA-HMCS (882, 747, 672, 568 and 344 mAh g^{-1}), S/Cd SA-HMCS (804, 670, 596, 479 and 300 mAh g^{-1}), and S/HMCS (453, 355, 276, 183 and 123 mAh g^{-1}). Owing to the orbital electron coupling between the Cd and Ga atoms, the reaction kinetics of the S/Ga-Cd DAs-HMCS cathode is significantly boosted, thereby displaying satisfactory rate performance. Even at a high specific current of 5 A g^{-1}, the S/Ga-Cd DAs-HMCS cathode still exhibits optimal performance among the literature for K-S batteries (Fig. 3e & Table S3)[6–8,15–17,39–42].

The S/Ga-Cd DAs-HMCS cathode with a high sulfur mass loading of 1.6 mg cm^{-2} was prepared to promote the practical application potential of K-S batteries. The S/Ga-Cd DAs-HMCS cathode with a high sulfur loading can exhibit stable cycling performance over 60 and 100 cycles at the specific currents of 0.2 and 0.5 A g^{-1}, respectively (Fig. 3f). Furthermore, the S/Ga-Cd DAs-HMCS cathode exhibited long-cycling stability, attaining a high reversible capacity of 649 mAh g^{-1} at 1 A g^{-1} after 500 cycles (Fig. 3g). Figure S31 displays the galvanostatic charge/discharge curves and cycling performance of the S/Ga-Cd DAs-HMCS cathode in the potential window of 0.5-2.8 V for K-ion batteries at 0.2 A g^{-1} and 1 A g^{-1}, showing the negligible charge capacity of 35.5 mAh g^{-1} after 100 cycles and 14.1 mAh g^{-1} after 500 cycles, respectively. The K-S pouch cell with S/Ga-Cd DAs-HMCS as the cathode and potassium metal as the anode could maintain the brightness of the light-emitting diode (LED) for an extended period, further proving the utility of the S/Ga-Cd DAs-HMCS cathode for K-S batteries (Fig. 3h).

To unveil the catalytic mechanism of the Ga-Cd atom pair, the reaction kinetics of the S/Ga-Cd DAs-HMCS, S/Ga SA-HMCS, S/Cd SA-HMCS, and S/HMCS were explored by CV tests at different scan rates of 0.2–0.8 mV s^{-1}, revealing a synergistic mechanism characterized by both diffusion-controlled and capacitive behaviors (Fig. S32–34)[43,44]. The strongest redox peaks are displayed for the S/Ga-Cd DAs-HMCS among the samples tested, confirming that the Ga-Cd atom pair can facilitate the conversion of potassium polysulfide. Compared with the three control samples, S/Ga-Cd DAs-HMCS (0.19 and 0.21) shows the largest slopes of I_p and $v^{0.5}$, signifying the fastest ion diffusion rate for the S/Ga-Cd DAs-HMCS cathode in K-S batteries (Fig. 4a & S35). As demonstrated by the SEM images of the S/Ga-Cd DAs-HMCS electrode after cycling, the HMCS host exhibits satisfactory structural stability during the charge and discharge process (Fig. S36).

As shown in Fig. 4b, the adsorption and UV-vis absorption experiments were conducted to ascertain the adsorbability of the S/Ga-Cd DAs-HMCS, S/Ga SA-HMCS, S/Cd SA-HMCS, and S/HMCS samples with respect to potassium polysulfide. The results indicate that the S/Ga-Cd DAs-HMCS with the Ga-Cd atom pair has a strong adsorption

https://doi.org/10.1038/s41467-025-63797-1

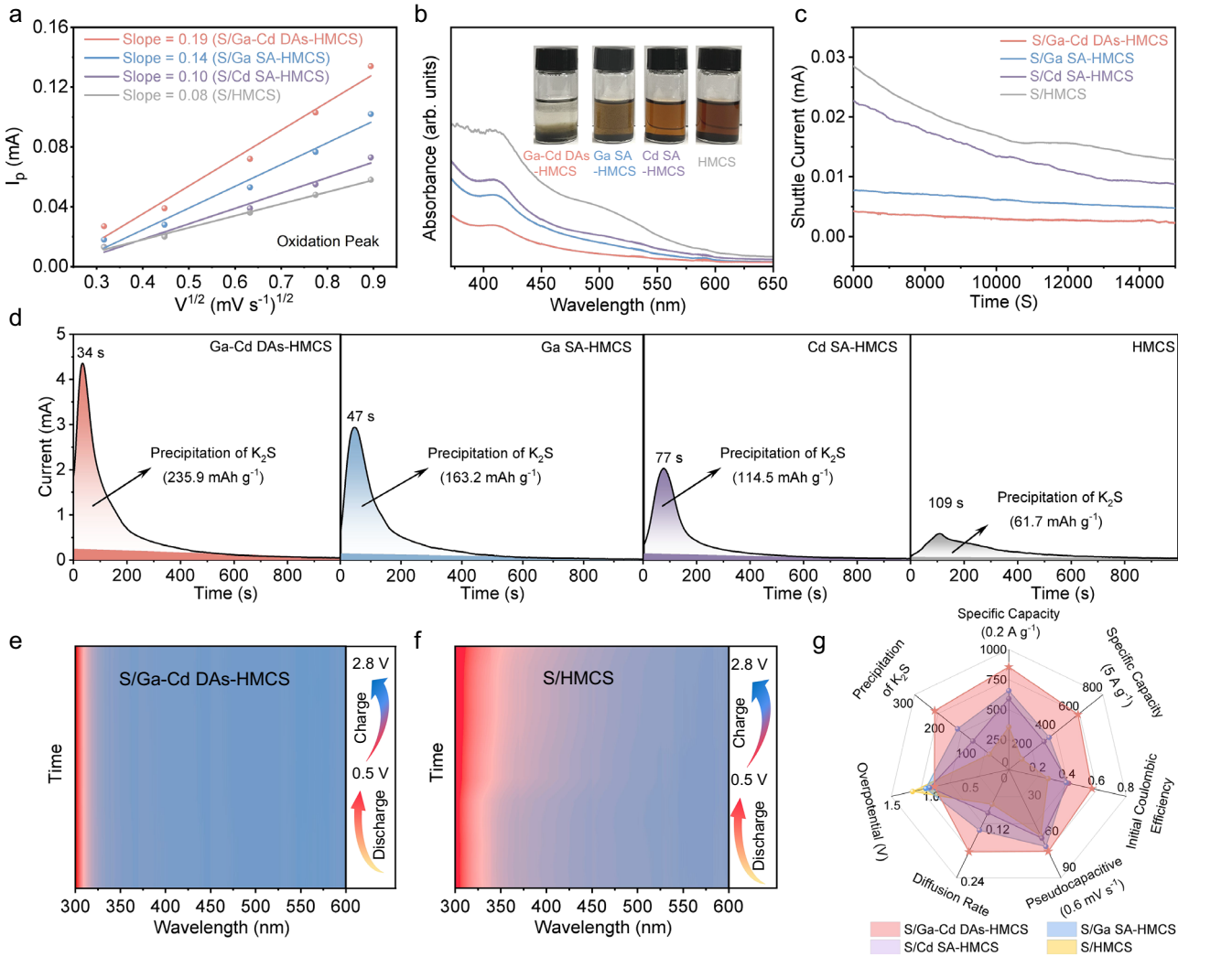

Fig. 4 | Analysis of the catalytic and adsorption capacity of Ga-Cd DAs-HMCS and three control groups. a Fitted lines of oxidation peak for S/Ga-Cd DAs-HMCS cathode and three control groups (S/Ga SA-HMCS, S/Cd SA-HMCS and S/HMCS) between I_p and $v^{1/2}$. **b** Optical photographs of visualized adsorption tests (K_2S_6) and UV-vis spectra of Ga-Cd DAs-HMCS, Ga SA-HMCS, Cd SA-HMCS and HMCS samples. **c** The shuttle currents of S/Ga-Cd DAs-HMCS cathode and three control groups. **d** The potentiostatic discharge curves of Ga-Cd DAs-HMCS, Ga SA-HMCS, Cd SA-HMCS and HMCS samples (K_2S_6-EC). **e**, **f** The in situ UV-vis spectra of S/Ga-Cd DAs-HMCS and S/HMCS cathodes during the first cycle (specific current of 0.2 A g^{-1}, test temperature of 28 °C). **g** Comparison of the radar chart for the S/Ga-Cd DAs-HMCS cathode and three control groups. Source data for **a**–**g** were provided as a Source Data file.

capacity for potassium polysulfide. Furthermore, the lowest shuttle current value observed for S/Ga-Cd DAs-HMCS (Fig. 4c) suggests that the Ga-Cd atom pair can provide optimal physical confinement and chemical anchoring for potassium polysulfide, thereby effectively mitigating the "shuttle effect" in K-S batteries. The enhanced kinetics of potassium polysulfide conversion endowed by the Ga-Cd atom pair catalyst is further evidenced by precipitation experiments via Faraday's law (Fig. 4d). Among the samples tested, the Ga-Cd DAs-HMCS exhibits the highest capacity of K_2S precipitation (235.9 mA h g^{-1}) and the fastest response time (34 s), surpassing those of the S/Ga SA-HMCS (163.2 mA h g^{-1} and 47 s), S/Ga SA-HMCS (114.5 mA h g^{-1} and 77 s) and S/HMCS (61.7 mA h g^{-1} and 109 s), which underscores the notable catalytic ability of Ga-Cd atom pair in the Ga-Cd DAs-HMCS for facilitating efficient solid-state potassium polysulfide conversion[45].

The enhanced adsorption and conversion capacity of potassium polysulfide by Ga-Cd atom pair, attributed to the orbital electron coupling of Cd single atoms, is evidenced by in situ UV spectra. During the charging and discharging process, no peaks related to the potassium polysulfide are detected for the S/Ga-Cd DAs-HMCS cathode, indicating a significant suppression of the "shuttle effect" in K-S batteries (Fig. 4e & S37a). In contrast, the distinct peaks of potassium polysulfide are observed during the charging and discharging processes in the in situ UV-vis spectra of the S/HMCS electrode (Fig. 4f & S37b). Consequently, the active sulfur in the S/Ga-Cd DAs-HMCS is fully converted into the K_2S, thereby improving the electrochemical performance of K-S batteries. The unique orbital electron coupling between the *p*-block Ga and *d*-block Cd enables the Ga-Cd atom pair to function as a comprehensive catalyst, facilitating both the catalysis and adsorption of potassium polysulfide while promoting the migration of K^+. As shown in Fig. 4g, the S/Ga-Cd DAs-HMCS outperforms the S/Ga SA-HMCS, S/Cd SA-HMCS and S/HMCS across several metrics, including initial CE, pseudocapacitance, diffusion rate, overpotential, and K_2S precipitation.

To gain insight into the mechanisms for the improved electrochemical catalytic efficiency of the Ga-Cd atom pair, we conducted a detailed investigation of the electronic structures and reaction pathways of Ga-Cd DAs-HMCS, Ga SA-HMCS, and Cd SA-HMCS using DFT calculations. The optimized model structure diagrams of the Ga-Cd DAs-HMCS, Ga SA-HMCS, Cd SA-HMCS, and K_2S_x (x = 8, 6, 4, 2, 1) were shown in Fig. S38 & 39 (Supplementary Data 1-8). As shown in Fig. S40,

https://doi.org/10.1038/s41467-025-63797-1

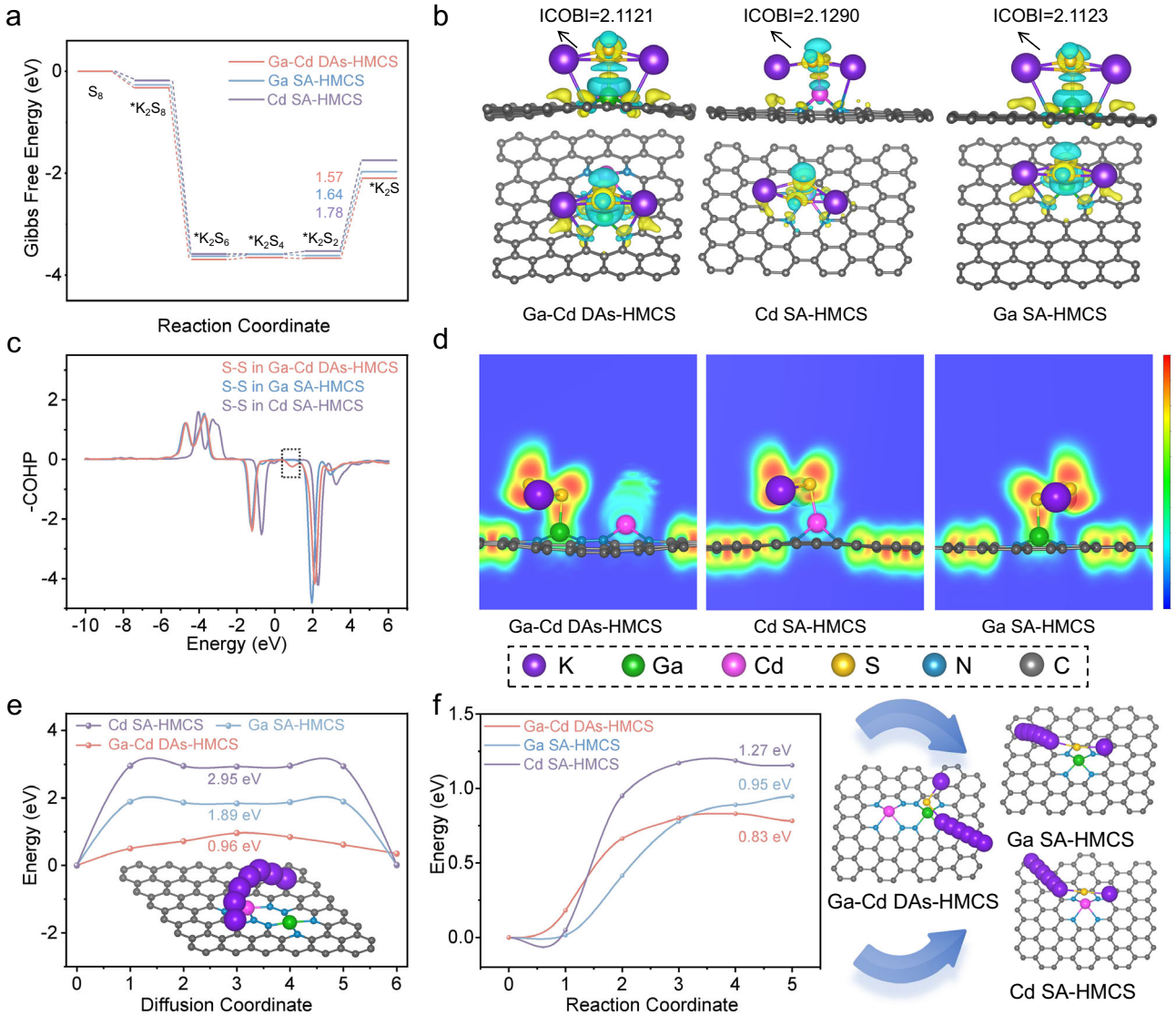

Fig. 5 | DFT calculations of Ga-Cd DAs-HMCS, Ga SA-HMCS, and Cd SA-HMCS. **a** Gibbs free energy profiles for the S_8 and K_2S_x (x = 8, 6, 4, 2, 1) on the Ga-Cd DAs-HMCS, Ga SA-HMCS, and Cd SA-HMCS models. **b** Charge density differences of K_2S_2 on Ga-Cd DAs-HMCS, Cd SA-HMC,S and Ga SA-HMCS surfaces. **c** COHP of S-S bond in K_2S_2 on Ga-Cd DAs-HMCS, Ga SA-HMC,S and Cd SA-HMCS surfaces. **d** ELF for K_2S adsorbed on Ga-Cd DAs-HMCS, Cd SA-HMCS and Ga SA-HMCS models. **e**, **f** Migrations energy of K-ion and energy barrier of K_2S dissociation on the Ga-Cd DAs-HMCS, Ga SA-HMCS and Cd SA-HMCS substrates. Source data for **a**, **c**, **e**, **f** were provided as a Source Data file.

the Ga-Cd DAs-HMCS configuration exhibits significantly stronger adsorption energy toward potassium polysulfide compared to Ga SA-HMCS and Cd SA-HMCS configurations, highlighting its strong anchoring capability for S_8 and K_2S_x. Figure 5a shows the Gibbs free energy changes associated with the reversible conversion reactions of S_8 and K_2S_x for the Ga-Cd DAs-HMCS, Ga SA-HMCS, and Cd SA-HMCS. The conversion of S_8 to K_2S_4 is thermodynamically spontaneous throughout the entire reaction process, whereas the conversion from K_2S_2 to K_2S is endothermic. Notably, the reaction sub-steps transitioning from K_2S_2 to K_2S must surmount the maximum energy barrier, which is identified as the rate-determining step in the overall reduction process. Compared with Ga SA-HMCS (1.64 eV) and Cd SA-HMCS (1.78 eV), the Ga-Cd DAs-HMCS (1.57 eV) displays a reduced reaction energy change, indicating that the Ga-Cd atom pair effectively lowers the Gibbs free energy change associated with the rate-determining step. This enhancement is attributed to the ability of the Ga site to acquire additional valence electrons through the orbital electron coupling with Cd, thereby activating the S-S bond in K_2S_2 and promoting the conversion of solid-phase K_2S_2 to K_2S. The DDEC analysis of K-S effective bond orders revealed weaker activation at the Ga-Cd atom pair (0.099) site compared to Ga (0.110) and Cd (0.127) sites, further promoting the conversion from K_2S_2 to K_2S conversion via K-S bond orders weakening (Table S4). Figure S41–43 show the optimized conformations of K_2S_x on the Ga-Cd DAs-HMCS, Cd SA-HMCS, and Ga SA-HMCS surfaces.

The introduction of Cd atomic site via the orbital electron coupling results in the adsorbed K_2S_2 on the Ga sites in Ga-Cd DAs-HMCS gaining more electrons compared to those in Ga SA-HMCS and Cd SA-HMCS (Fig. 5b). This is evidenced by the lower integrated crystal orbital bond index (ICOBI) for K_2S_2 on Ga-Cd DAs-HMCS relative to that on Ga SA-HMCS and Cd SA-HMCS. The S-S bond of K_2S_2, adsorbed on Ga sites, experiences a loss of electrons, indicating effective coordination between sulfur and the active site. As shown in Fig. 5c, the crystal orbital Hamilton population (COHP) of S-S bond in K_2S_2 on the three model surfaces was calculated for further analysis. This analysis reveals that the Ga site on the Ga-Cd DAs-HMCS surface is closest to the Fermi level among the antibonding states near the Fermi energy level of the S-S bonds in K_2S_2, proving that Ga is more conducive to

https://doi.org/10.1038/s41467-025-63797-1

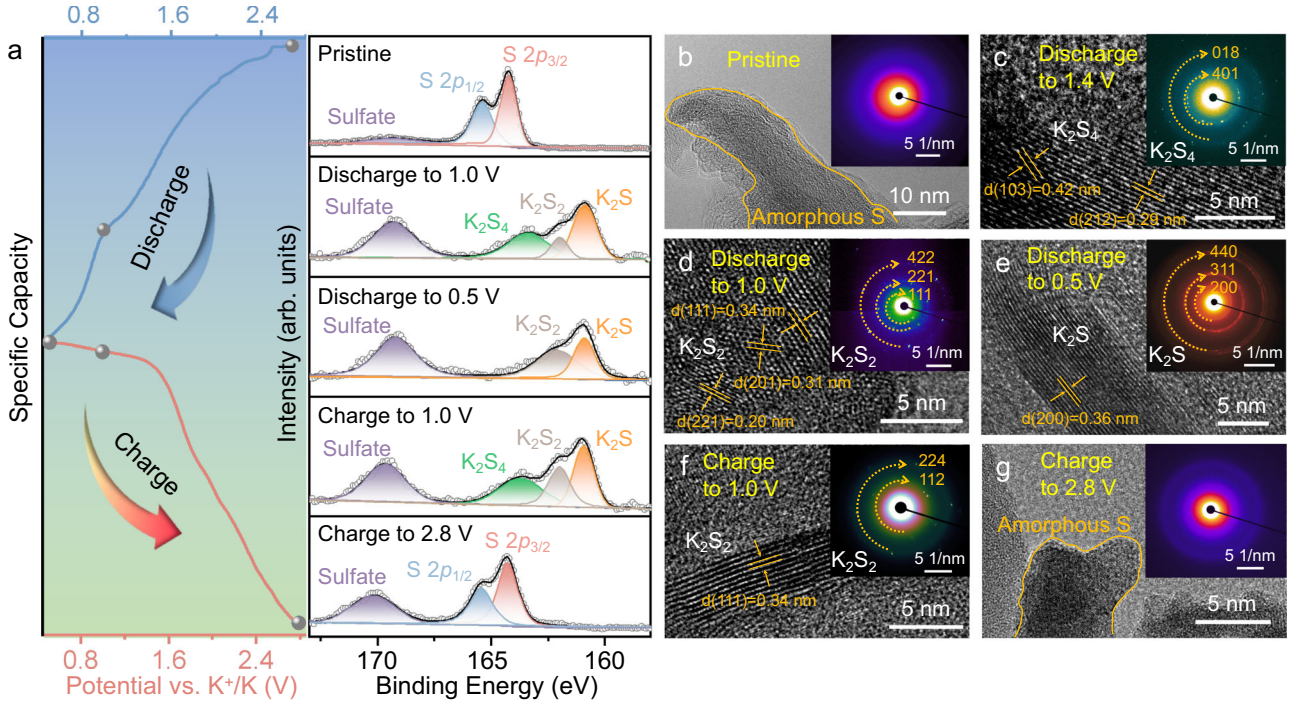

Fig. 6 | Electrochemical mechanism of K-S battery based on S/Ga-Cd DAs-HMCS. **a** Ex situ high-resolution XPS spectra of S/Ga-Cd DAs-HMCS electrode. **b**–**g** Ex situ HRTEM and SAED images of S/Ga-Cd DAs-HMCS electrode during the initial discharge/charge processes. The batteries for ex situ measurement were tested under different charge/discharge states during the first cycle, with a specific current of 0.05 A g^{-1} and a test temperature of 28 °C. Source data for **a** were provided as a Source Data file.

activating the S-S bond in K_2S_2. The electron localization functions (ELF) further confirm that K_2S_2 is adsorbed on Ga site, with a notable bonding interaction between Ga and S, demonstrating the satisfactory catalytic ability of Ga as the active site in Ga-Cd DAs-HMCS for K_2S_2 (Fig. 5d). A comparative analysis of the DOS of the K_2S_2 and K_2S_2 adsorbed on the three models reveals that the DOS of K_2S_2 on the Ga-Cd DAs-HMCS surface undergoes a downward shift toward deeper energy levels (Fig. S44). This observation demonstrates that Cd in the Ga-Cd DAs-HMCS further facilitates electron transfer from Ga to K_2S_2, thus activating the K_2S_2 molecule through orbital electron coupling. Additionally, the migration barriers of K-ions on the surfaces of Ga-Cd DAs-HMCS, Ga SA-HMCS and Cd SA-HMCS were calculated to be 0.96, 1.89 and 2.95 eV, respectively, implying that K-ion migration occurs most rapidly on the Ga-Cd DAs-HMCS surface (Fig. 5e). The energy barriers for K_2S decomposition on the surfaces of Ga-Cd DAs-HMCS (0.83 eV), Ga SA-HMCS (0.95 eV) and Cd SA-HMCS (1.27 eV) are compared (Fig. 5f). The lowest energy barrier for K_2S decomposition on the Ga-Cd DAs-HMCS surface suggests that Ga-Cd atom pair can accelerate the transformation of K_2S.

To explore the conversion mechanism and the reaction products of sulfur and potassium polysulfide in K-S batteries under the catalysis of Ga-Cd atom pair, a series of characterization techniques were employed. Figure S45 presents the in situ XRD results of the S/Ga-Cd DAs-HMCS cathode during the initial discharge and charge processes for K-S batteries. During the discharging process, the characteristic peaks of S_8 (JCPDF No. 78-1888) gradually disappear. In the following charging process, the characteristic peaks of S_8 re-emerged, indicating a highly reversible conversion process of S_8[16,19]. Moreover, the ex situ high-resolution XPS characterizations of S/Ga-Cd DAs-HMCS cathode were conducted to further define the conversion products of sulfur (Fig. 6a). We found that during the pristine and discharging stages, the diffraction peaks of S_8, K_2S_4, K_2S_2 and K_2S were detected in succession, and in the subsequent charging stages, a reversible transformation of $S_8 \rightarrow K_2S_4 \rightarrow K_2S_2 \rightarrow K_2S$ occurred[5,17]. To further validate these reversible reactions from S_8 to K_2S, we conducted ex situ HRTEM and selected area electron diffraction (SAED) of the S/Ga-Cd DAs-HMCS cathode for K-S batteries. Figure 6b shows the sulfur exhibiting an amorphous structure at the initial stage. As the battery discharges to 1.4, 1.0, and 0.5 V, the lattice spacings and diffraction rings of K_2S_4, K_2S_2, and K_2S are detected, respectively (Fig. 6c–e). Subsequently, upon charging the battery to 1.0 and 2.8 V, the lattice spacings and diffraction rings of K_2S_2 and amorphous sulfur are re-identified (Fig. 6f, g). The final results of ex situ high-resolution XPS, HRTEM, and SAED align well with the in situ XRD, clearly identifying the reaction intermediates of K_2S_2 and K_2S, which indicates that the Ga-Cd atom pair can promote the solid-state conversion of K_2S_2 to K_2S during the cycling process, thereby enhancing the conversion efficiency of reactive sulfur for K-S batteries.

We report a class of Ga-Cd atom pairs with strong orbital electron coupling between Ga and Cd, anchored on HMCS for facilitating the conversion of solid-phase K_2S_2 to K_2S in K-S batteries. DFT calculations and high-resolution XPS spectra indicate that the *d*-block Cd with a more filled valence electron configuration could transfer more electrons to the empty orbitals of the *p*-block Ga. Therefore, the Ga site with strong adsorption capacity for potassium polysulfide serves as the catalytic active center, activating the S-S bond through the participation of additional valence electrons, thus lowering the conversion energy barrier of solid-state potassium polysulfide and increasing the utilization of active sulfur. The unique orbital electron coupling between the *p*-block Ga and *d*-block Cd enables the S/Ga-Cd DAs-HMCS cathode to exhibit considerably long cycle stability and the highest discharge capacity of 589 mAh g^{-1} at a specific current of 5 A g^{-1} among the reported literature on K-S batteries. The in situ UV-vis spectra and precipitation experiments demonstrate that the Ga-Cd DAs-HMCS catalyst can effectively inhibit the dissolution and "shuttle effect" of potassium polysulfide, thereby accelerating the kinetics of K-S batteries.

Methods

Chemicals

Tetraethylorthosilicate (TEOS, AR), ethanol (AR, ≥99.7%), and sodium hydroxide (NaOH, AR, ≥95%) were purchased from Beijing Tongguang Fine Chemicals Company. Formaldehyde solution (AR, 40%) was purchased from Adamas-beta. Ammonia solution ($NH_3{\cdot}H_2O$, 30 wt%), gallium(III) nitrate hydrate ($Ga(NO_3)_3{\cdot}3H_2O$, ≥99%), cadmium nitrate tetrahydrate ($Cd(NO_3)_2{\cdot}4H_2O$, ≥99%), sulfur (99.999%) and potassium metal (99.5%) were purchased from Shanghai Aladdin Biochemical Technology Co., Ltd. M-aminophenol (AR, 99%) was purchased from innochem. Potassium bis(trifluoromethylsulfonyl) imide (KTFSI, battery grade, ≥99.5%), ethylene carbonate (EC, battery grade, ≥99.95%), carboxymethyl cellulose (CMC, battery grade) binder, and acetylene black (battery grade) were purchased from DoDoChem.

Synthesis of the Ga-Cd DAs-HMCS, Ga SA-HMCS, Cd SA-HMCS and HMCS

In a typical synthesis process, a SiO_2 suspension was prepared by sequentially dissolving 15 mL of ammonia solution and 17.3 mL of tetraethylorthosilicate (TEOS) in a mixed solvent of 350 mL ethanol and 50 mL deionized water, followed by 10 min of magnetic stirring. Subsequently, 150 mg of $Ga(NO_3)_3$ was introduced into the SiO_2 suspension under continuous stirring for 10 min. Then, 2.8 mL of formaldehyde solution and 2.1 g of *M*-aminophenol were added, and the mixture was vigorously stirred for 12 h at about 28 °C. Afterward, 150 mg of $Cd(NO_3)_2$ was incorporated, and stirring was maintained for an additional 12 h. The resulting precipitate was washed via centrifugation with deionized water and ethanol, followed by vacuum drying at 60 °C for 12 h to obtain Ga-Cd SiO_2@APF. The sample was then calcinated at 700 °C for 5 h under an Ar atmosphere to produce Ga-Cd SiO_2@C nanospheres. To obtain Ga-Cd@HMCS, the silica template was etched using a 1.5 M NaOH solution. The Ga-Cd@HMCS mixed ice was melted at room temperature after irradiation by Xe-lamp (λ > 420 nm). The Ga-Cd DAs-HMCS was obtained by vacuum freeze-drying. The Ga-Cd DAs-HMCS sample was chemically activated by mixing with KOH, followed by calcination at 800 °C for 30 min under an Ar atmosphere. The Ga SA-HMCS and Cd SA-HMCS were also synthesized by the same method, with the addition of 300 mg of $GaNO_3$ and 300 mg of $CdNO_3$, respectively.

Synthesis of the S/Ga-Cd DAs-HMCS, S/Ga SA-HMCS, S/Cd SA-HMCS and S/HMCS cathodes

The Ga-Cd DAs-HMCS (Ga SA-HMCS, Cd SA-HMCS, and HMCS) and sulfur were mixed in a 1:1 mass ratio using mortar-pestle. The mixture (without solvent addition) was sealed in an Ar-filled autoclave and heated at 155 °C for 12 h to obtain the S/Ga-Cd DAs-HMCS, S/Ga SA-HMCS, S/Cd SA-HMCS, and S/HMCS cathodes.

Preparation of K_2S_6 solution

A stoichiometric mixture of sulfur and anhydrous K_2S powder was dispersed in EC solution and stirred at 60 °C for 24 h in an Ar-filled glove box. The resulting dark brown solution contained 0.1 M atomic sulfur in the form of K_2S_6.

K_2S precipitation experiments

Precipitation experiments of K_2S were conducted using CR2032-type coin cells with a GF/D membrane as the separator, carbon cloth as current collector and K metal as the anode. A volume of 50 µL of K_2S_6 catholyte was applied to the surfaces of Ga-Cd DAs-HMCS, Ga SA-HMCS, Cd SA-HMCS and HMCS electrodes, while 80 µL of EC electrolyte without K_2S_6 was dropped on the negative electrode at 35 °C. The assembled batteries were initially galvanostatically discharged to 1.30 V at 35 °C, followed by a potentiostatic hold at 1.25 V to promote K_2S nucleation and growth. The potentiostatic discharge was maintained until the current decayed below 10^{-7} A.

Electrochemical measurements

All electrochemical measurements were conducted using CR2032-type coin cells in an Ar-filled glove box (MIKROUNA, $H_2O \le 0.01$ ppm, $O_2 \le 0.01$ ppm) at 26 ± 3 °C. The coin cell case, gasket, and funnel-type spring tab were fabricated from 304 stainless steel. The working electrode was prepared by mixing the active material, carboxymethyl cellulose (CMC) binder, and acetylene black conductive agent at a mass ratio of 7:2:1 in deionized water, followed by coating the mixture onto carbon-coated Al foil (0.016 mm thick) via a doctor blade. The electrolyte was prepared by dissolving 3 M potassium bis(trifluoromethylsulfonyl)imide (KTFSI) in ethylene carbonate (EC). The obtained working electrodes (single-sided coated) were dried under vacuum at 70 °C for 12 h. K metal was used as the counter and reference electrodes, and GB/D was employed as the separator with a size of approximately 2 cm^2. In the K-S batteries, the size of all cathodes was approximately 0.5 cm^2. The K metal electrode (0.2 mm thick) was tailored into pieces of 0.5 cm^2 in an argon-filled glove box. The sulfur mass loading in the conventional and thick electrodes was approximately 0.6 and 1.6 mg cm^{-2}, respectively. The capacity value was calculated based on the mass of sulfur. The electrolyte/sulfur (E/S) ratio of the thick electrode for the K-S batteries is about 31.3 µL mg^{-1}. Galvanostatic charge-discharge tests were conducted on the Neware BTS-610 instrument within a potential window of 0.5–2.8 V. Cyclic voltammetry (CV) measurements were conducted on a CHI 660D workstation with scan rates of 0.1, 0.2, 0.4, 0.6, and 0.8 mV s^{-1}, over a potential range of 0.5-2.8 V. All battery tests were performed at about 28 °C after aging for 5 hours.

Material characterization

TEM was conducted on a HITACHI H-7700 at an accelerating voltage of 100 kV. Atomic-resolution HAADF-STEM and corresponding elemental analysis were performed on a JEM ARM300F TEM. HRTEM and SAED were performed on a JEM-2100F. SEM was performed on a ZEISS G450, with a beam voltage of 5 kV employed. XRD patterns were collected on a PANalytical-XRD instrument using a Cu Kα radiation (λ = 0.15406 nm), operating at 40 kV and a current of 30 mA. Data were acquired at a scan rate of 15° min^{-1} and a step size of 0.01°. XPS measurements were carried out on a Kratos Axis Supra$^+$ spectrometer equipped with a monochromatic Al Kα excitation source (1486.6 eV) and a high-resolution hemispherical analyzer. The source power was maintained at 150 W during data acquisition, which employed a hybrid operational mode covering an analytical area of 700 × 300 µm. Survey spectra were acquired at 160 eV pass energy (1.0 eV/step), whereas high-resolution regional spectra utilized 40 eV pass energy (0.1 eV/step)[46]. A charge neutralizer with low-energy electrons was used to exclude surface charging effects, and the C 1 s peak (284.8 eV) was used as a reference for binding energy calibration. TGA was conducted on a NETZSCH TG 209 F3 Tarsus under an N_2 atmosphere from 30 °C to 600 °C with a heating rate of 10 °C min^{-1} to determine the sulfur contents of samples.

XAFS spectra at the Ga K-edge and Cd K-edge of Ga-Cd DAs-HMCS, Ga SA-HMCS and Cd SA-HMCS were collected at the BL14W1 and BL11B in the Shanghai Synchrotron Radiation Facility (SSRF). The Ga K-edge and Cd K-edge XAFS data were recorded in a transmission mode. Ga foil, Ga_2O_3, Cd foil and CdO were used as reference standards. The acquired EXAFS data was processed using the Athena module of the IFEFFIT software[47]. The k^2 weighted XAFS were obtained by subtracting the pre-edge and post-edge background from the raw absorption data, followed by normalization to the edge jump step (derived from the first derivative of the absorption edge) in Athena software. The χ(k) data were Fourier transformed to R-space for

further analysis. XAFS fitting was proceeded using ARTEMIS software[47]. The EXAFS equation can be expressed as:

$$\chi(k) = \sum_j \frac{N_j S_0^2 F_j(k)}{kR_j^2} \exp\left(-2k^2\sigma^2\right) \exp\left(\frac{-2R_j}{\lambda(k)}\right) \sin\left[2kR_j + \Phi_j(k)\right]$$

where the parameters denote: S_0^2 denotes the amplitude reduction factor, $F_j(k)$ represents the effective curved-wave backscattering amplitude, N_j corresponds to the coordination number of the jth atomic shell, R_j represents the interatomic distance between the absorbing atom and the scattering atoms within the jth shell, λ stands for the mean free path in Å, $\Phi_j(k)$ represents the total phase shift, which incorporates the phase shift for each shell and the total central atom phase shift, and σ_j is the Debye-Waller parameter for the jth atomic shell, reflecting the variation of interatomic distances around the average R_j and representing the ordering degree of the materials[48]. The relevant parameters were calculated with the ab initio code FEFF 6. Wavelet transformed (WT) analysis of EXAFS data was conducted using the HAMA software[49,50]. The R space is between 0 and 6 Å. The calculating pattern is Morlet. The kappa Morlet $\kappa = 10$, the sigma Morlet $\sigma = 1$.

Ex situ measurements

Battery assembly was performed following the identical procedure employed for electrochemical measurements. The batteries were cycled to a predetermined voltage at a current density of 0.1 A g^{-1} before being disassembled. The harvested electrode sheets were subsequently immersed in dimethyl carbonate (DMC) for 5 min, followed by drying in an argon-filled glove box. For ex situ high-resolution XPS measurements, the electrode sheets were sectioned into small pieces and affixed to the sample stage of an XPS vacuum transfer device at 26 ± 3 °C for testing. For ex situ HRTEM and SAED measurements, the electrode sheets were ultrasonically dispersed in DMC, and the resulting suspension was dropped onto a microgrid at 26 ± 3 °C for testing.

Theoretical Calculation

DFT calculations were performed using the Vienna Ab initio Simulation Package (VASP)[51]. The energy calculations were conducted with the Revised Perdew-Burke-Ernzerhof functional[52,53], while the electronic structure calculations employed the hybrid functional HSE06[54]. Geometry structures were optimized with a cutoff energy of 500 eV. To account for the solvent stabilization on reaction intermediates, implicit solvation was incorporated using the VASPsol software package[55], with EC (dielectric constant of 89.6) selected as the solvent. The projector-augmented wave (PAW) pseudo-potentials were used to describe the electronic exchange interactions[56]. The energy convergence threshold of 10^{-5} eV and geometry relaxation of 0.02 eV/Å were applied. A Monkhorst-Pack k-point mesh of 3 × 3 × 1 was adopted for Brillouin zone sampling. A vacuum layer of 15 Å in the normal direction was employed to separate neighboring slabs. Transition states were located using the CI-NEB method[57]. Bond order analysis was performed via the DDEC6 method, which involves calculating the bond orders based on the electron density distribution to gain insights into the bonding characteristics of the system under study[58].

Data availability

The data that support the conclusions of this study are available within the paper and Supporting information. Source data are provided with this paper.

References

1. Kovalenko, I. et al. A major constituent of brown algae for use in high-capacity Li-ion batteries. *Science* **334**, 75–79 (2011).
2. Armand, M. & Tarascon, J. M. Building better batteries. *Nature* **451**, 652 (2008).
3. Dunn, B., Kamath, H. & Tarascon, J. M. Electrical energy storage for the grid: a battery of choices. *Science* **334**, 928–935 (2011).
4. Grey, C. P. & Tarascon, J. M. Sustainability and in situ monitoring in battery development. *Nat. Mater.* **16**, 45–56 (2016).
5. Wang, B. et al. An energetic K^+-S aqueous battery with 96% sulfur redox utilization. *Joule* **8**, 2033–2048 (2024).
6. Jiang, Z. et al. Anion-regulated sulfur conversion in high-content carbon layer confined sulfur cathode maximizes voltage and rate capability of K-S batteries. *Adv. Mater.* **36**, 2311127 (2024).
7. Ye, S. et al. Boosting the "Solid-Liquid-Solid" conversion reaction via bifunctional carbonate-based electrolyte for ultra-long-life potassium-sulfur batteries. *Angew. Chem. Int. Ed.* **62**, e202307728 (2023).
8. Ye, C. et al. Reducing overpotential of solid-state sulfide conversion in potassium-sulfur batteries. *Angew. Chem. Int. Ed.* **62**, e202301681 (2023).
9. Zhou, S. et al. Visualizing interfacial collective reaction behaviour of Li-S batteries. *Nature* **621**, 75 (2023).
10. Li, Z. et al. Lithiated metallic molybdenum disulfide nanosheets for high-performance lithium-sulfur batteries. *Nat. Energy* **8**, 84–93 (2023).
11. Hua, W. et al. Optimizing the p charge of S in p-block metal sulfides for sulfur reduction electrocatalysis. *Nat. Catal.* **6**, 174–184 (2023).
12. Fang, R., Xu, J. & Wang, D.-W. Covalent fixing of sulfur in metal-sulfur batteries. *Energy Environ. Sci.* **13**, 432–471 (2020).
13. Ding, J. et al. Review of emerging potassium-sulfur batteries. *Adv. Mater.* **32**, 1908007 (2020).
14. Zhang, E. et al. Single-atom Yttrium engineering Janus electrode for rechargeable Na-S batteries. *J. Am. Chem. Soc.* **144**, 18995–19007 (2022).
15. Ye, C. et al. Catalytic oxidation of K_2S via atomic Co and Pyridinic N synergy in potassium-sulfur batteries. *J. Am. Chem. Soc.* **143**, 16902–16907 (2021).
16. Zhang, S. Strong d-π orbital coupling of Co-C_4 atomic sites on Graphdiyne boosts potassium-sulfur battery electrocatalysis. *J. Am. Chem. Soc.* **146**, 4433–4443 (2024).
17. Song, W. et al. Optimizing potassium polysulfides for high-performance potassium-sulfur batteries. *Nat. Commun.* **15**, 1005 (2024).
18. Bai, R. et al. Toward complete transformation of sodium polysulfides by regulating the second-shell coordinating environment of atomically dispersed Fe. *Angew. Chem. Int. Ed.* **62**, e202218165 (2023).
19. Gu, S. et al. Chemical synthesis of K_2S_2 and K_2S_3 for probing electrochemical mechanisms in K-S batteries. *ACS Energy Lett.* **3**, 2858–2864 (2018).
20. Kumar, V., Saroja, A. P. & Xu, Y. Carbon materials for Na-S and K-S batteries. *Matter* **5**, 808–836 (2022).
21. Shao, J. et al. K_3SbS_4 as a potassium superionic conductor with low activation energy for K-S batteries. *Angew. Chem. Int. Ed.* **61**, e202200606 (2022).
22. Lee, S. et al. High-energy and long-lifespan potassium-sulfur batteries enabled by concentrated electrolyte. *Adv. Funct. Mater.* **32**, 2209145 (2022).
23. Zhao, Q. et al. Photo-induced synthesis of heteronuclear dual-atom catalysts. *Nat. Synth.* **3**, 497–506 (2024).
24. Ballesteros-Soberanas, J. et al. A MOF-supported Pd_1-Au_1 dimer catalyses the semihydrogenation reaction of acetylene in ethylene with a nearly barrierless activation energy. *Nat. Catal.* **7**, 452–463 (2023).
25. Hao, Q. et al. Nickel dual-atom sites for electrochemical carbon dioxide reduction. *Nat. Synth.* **1**, 719–728 (2022).
26. Zhang, S. et al. Fe/Cu diatomic catalysts for electrochemical nitrate reduction to ammonia. *Nat. Commun.* **14**, 3634 (2023).

27. Xie, Z. et al. Well-defined diatomic catalysis for photosynthesis of C_2H_4 from CO_2. *Sci. Adv.* **8**, eabm3779 (2022).
28. Han, L. et al. Design of Ru-Ni diatomic sites for efficient alkaline hydrogen oxidation. *Angew. Chem. Int. Ed.* **62**, e202302829 (2023).
29. Zhang, Z. et al. Liquid Fluxional Ga single atom catalysts for efficient electrochemical CO_2 reduction. *Angew. Chem. Int. Ed.* **62**, e202215136 (2023).
30. Sun, L. et al. Photocatalytic reductive C-O bond scission promoted by low-work-function Cd single atoms and clusters. *Chem. Commun.* **59**, 2102–2105 (2023).
31. Tan, H. et al. Photocatalysis of water into hydrogen peroxide over an atomic Ga-N_5 site. *Nat. Synth.* **2**, 557–563 (2023).
32. Tao, L. et al. Precise synthetic control of exclusive ligand effect boosts oxygen reduction catalysis. *Nat. Commun.* **14**, 6893 (2023).
33. Jiang, W. et al. Photocatalyst for high-performance H_2 production: ga-doped polymeric carbon nitride. *Angew. Chem. Int. Ed.* **60**, 6124–6129 (2021).
34. Zhang, M. et al. Highly active and selective electroreduction of N_2 by the catalysis of Ga single atoms stabilized on amorphous TiO_2 nanofibers. *ACS Nano* **16**, 4186–4196 (2022).
35. Zhang, X. et al. In-situ-formed Cd and Ag_2S decorated CdS photocatalyst with boosted charge carrier spatial separation for enhancing UV-vis-NIR photocatalytic hydrogen evolution. *Appl. Catal. B: Environ.* **298**, 120620 (2021).
36. Chen, Y. et al. Coordination shell dependent activity of CuCo diatomic catalysts for oxygen reduction, oxygen evolution, and hydrogen evolution reaction. *Adv. Funct. Mater.* **34**, 2311664 (2023).
37. Zhang, J. et al. Novel (Pt-O_x)-(Co-O_y) nonbonding active structures on defective carbon from oxygen-rich coal tar pitch for efficient HER and ORR. *Adv. Mater.* **34**, 2206960 (2022).
38. Jiao, L. et al. Non-Bonding interaction of neighboring Fe and Ni single-atom pairs on MOF-derived N-doped carbon for enhanced CO_2 electroreduction. *J. Am. Chem. Soc.* **143**, 19417–19424 (2021).
39. Hu, L. et al. A superficial sulfur interfacial control strategy for the fabrication of a sulfur/carbon composite for potassium-sulfur batteries. *Chem. Commun.* **57**, 1490–1493 (2021).
40. Ge, X. et al. Metal-organic framework-derived nitrogen-doped cobalt nanocluster inlaid porous carbon as high-efficiency catalyst for advanced potassium-sulfur batteries. *ACS Nano* **14**, 16022–16035 (2020).
41. Yang, K. et al. Binder-free and high-loading cathode realized by hierarchical structure for potassium-sulfur batteries. *Small Methods* **6**, 2100899 (2021).
42. Zhao, X. et al. High performance potassium-sulfur batteries and their reaction mechanism. *J. Mater. Chem. A* **8**, 10875–10884 (2020).
43. Wei, X. et al. Three-dimensional hierarchically porous MoS_2 foam as high-rate and stable lithium-ion battery anode. *Nat. Commun.* **13**, 6006 (2022).
44. Zhang, S. et al. An open-ended Ni_3S_2-Co_9S_8 heterostructures nanocage anode with enhanced reaction kinetics for superior potassium-ion batteries. *Adv. Mater.* **34**, 2201420 (2022).
45. Zhang, S. et al. Mo_2N-W_2N heterostructures embedded in spherical carbon superstructure as highly efficient polysulfide electrocatalysts for stable room-temperature Na-S batteries. *Adv. Mater.* **33**, 2103846 (2021).
46. Nandasiri, M. et al. In situ chemical imaging of solid-electrolyte interphase layer evolution in Li-S batteries. *Chem. Mater.* **29**, 4728–4737 (2017).
47. Ravel, B. & Newville, M. ATHENA, ARTEMIS, HEPHAESTUS: data analysis for X-ray absorption spectroscopy using IFEFFIT. *J. Synchrotron. Radiat.* **12**, 537–541 (2005).
48. Shi, Q. et al. Single-atom Sn-Zn pairs in CuO catalyst promote dimethyldichlorosilane synthesis. *Natl Sci. Rev.* **7**, 600–608 (2020).
49. Funke, H. et al. A new FEFF-based wavelet for EXAFS data analysis. *J. Synchrotron. Radiat.* **14**, 426–432 (2007).
50. Funke, H. et al. Wavelet analysis of extended X-ray absorption fine structure data. *Phys. Rev. B* **71**, 094110 (2005).
51. Kresse, G. & Furthmüller, J. Efficiency of ab-initio total energy calculations for metals and semiconductors using a plane-wave basis set. *Comput. Mater. Sci.* **6**, 15–50 (1996).
52. Hammer, B. et al. Improved adsorption energetics within density-functional theory using revised Perdew-Burke-Ernzerhof functionals. *Phys. Rev. B* **59**, 7413 (1999).
53. Perdew, J. P. et al. Generalized gradient approximation made simple. *Phys. Rev. Lett.* **77**, 3865–3868 (1996).
54. Perdew, J. et al. Restoring the density-gradient expansion for exchange in solids and surfaces. *Phys. Rev. Lett.* **100**, 136406 (2008).
55. Mathew, K. et al. Implicit solvation model for density-functional study of nanocrystal surfaces and reaction pathways. *J. Chem. Phys.* **140**, 084106 (2014).
56. Kresse, G. & Joubert, D. From ultrasoft pseudopotentials to the projector augmented-wave method. *Phys. Rev. B* **59**, 1758–1775 (1999).
57. Sheppard, D. et al. A generalized solid-state nudged elastic band method. *J. Chem. Phys.* **136**, 074103 (2012).
58. Manz, T. & Limas, N. Introducing DDEC6 atomic population analysis: part 1. Charge partitioning theory and methodology. *RSC Adv.* **6**, 47771–47801 (2016).

Acknowledgements

This study was financially supported by Beijing Natural Science Foundation (No. Z220020(S.G.)), National Key R&D Program of China (No. 2022YFE0128500, 2024YFE0109200, 2024YFA1410000), Ministry of Science and Technology of China (2018YFA0703502(J.Z.) and 2016YFA0200104(J.Z.)), National Science Fund for Distinguished Young Scholars (No. 52025133(S.G.), 52525203(Y.Y.)), National Natural Science Foundation of China (52261135633(S.G.), 52525203(Y.Y.), 52394170(Y.Y.), 52394171(Y.Y.), U24A2067(Y.Y.), 52202201(S.Z.), 52574359(S.Z.) 22309006(Y.G.)), the Fundamental Research Funds for the Central Universities (WK9990000170(Y.Y.)), China National Petroleum Corporation-Peking University Strategic Cooperation Project of Fundamental Research, New Cornerstone Science Foundation through the XPLORER PRIZE, CNPC Innovation Found (2021DQ02-1002(S.G.)), the National Postdoctoral Program for Innovative Talents (BX20220015(S.Z.)), and the China Postdoctoral Science Foundation (2022M720002(S.Z.)). The authors thank the photoemission photoendstations BL14W1 and BL11B in the Shanghai Synchrotron Radiation Facility (SSRF) for the help with characterizations.

Author contributions

S.Z. and Z.L. contributed equally to this paper. S.Z. and S.G. conceived the original idea and designed the project. S.Z. and Z.L. performed the experiments. S.G., J.Z., Y.Y., and M.Luo supervised the experiments and edited this paper. M.Li and Y.G. contributed to the DFT calculation parts. Y.H., R.Z., L.T., Y.L,. and N.Y. collected and analyzed the experimental data. X.H. and X.Z. conducted HAADF-STEM and data analyses. All authors discussed the results and commented on the manuscript.

Competing interests

The authors declare no competing interests.

Additional information

Supplementary information The online version contains supplementary material available at https://doi.org/10.1038/s41467-025-63797-1.

Correspondence and requests for materials should be addressed to Yan Yu, Shaojun Guo or Jin Zhang.

Peer review information *Nature Communications* thanks [Md Mahbubul Islam and the other, anonymous, reviewer(s) for their contribution to the peer review of this work. A peer review file is available.